

Article

# A Wigner Function Approach to Coherence in a Talbot-Lau Interferometer

Eric Imhof<sup>1,2,\*</sup>, James Stickney<sup>1</sup> and Matthew Squires<sup>3</sup>

<sup>1</sup> Space Dynamics Laboratory, Utah State University Research Foundation, North Logan, UT 84341, USA; james.stickney@sdl.usu.edu

<sup>2</sup> Kirtland Air Force Base, Albuquerque, NM 87117, USA

<sup>3</sup> U.S. Air Force Research Laboratory, Kirtland Air Force Base, Albuquerque, NM 87117, USA; Matthew.Squires@kirtland.af.mil

\* Correspondence: eric.imhof@sdl.usu.edu

Academic Editors: A. Kumarakrishnan and Dallin S. Durfee

Received: 3 May 2016; Accepted: 16 June 2016; Published: 22 June 2016

**Abstract:** Using a thermal gas, we model the signal of a trapped interferometer. This interferometer uses two short laser pulses, separated by time  $T$ , which act as a phase grating for the matter waves. Near time  $2T$ , there is an echo in the cloud's density due to the Talbot-Lau effect. Our model uses the Wigner function approach and includes a weak residual harmonic trap. The analysis shows that the residual potential limits the interferometer's visibility, shifts the echo time of the interferometer, and alters its time dependence. Loss of visibility can be mitigated by optimizing the initial trap frequency just before the interferometer cycle begins.

**Keywords:** trapped atom interferometry; Wigner function; Talbot-Lau interferometer; coherence time

## 1. Introduction

Cold atom interferometry has been investigated for precision measurement applications [1,2], particularly inertial navigation [3–6]. Atom interferometers have demonstrated orders of magnitude improvement in bias stability over commercial navigation grade ring laser gyroscopes [7] and similar gains are expected for accelerometers, gravimeters, magnetometers, and more.

Transitioning the technology to a real-world device has proven difficult. The most sensitive atom interferometers use a 10-meter long apparatus [8]. These measurements rely on a Raman pulse technique which changes the internal state of the interrogated atoms. Because of the difficulty in confining multiple states with a magnetic field, atoms are allowed to propagate freely, necessitating a large system.

Single internal state splitting has allowed atoms to be trapped for the duration of the interferometer cycle, reducing the apparatus length to a few millimeters [9]. Techniques for confined splitting include double-well potentials [10], optical lattices [11], and standing wave pulses [12,13]. However, these interferometers have used Bose-Einstein condensates, which require cooling stages that increase power consumption, decrease possible repetition rates, and lower atom numbers.

One single state technique has been shown to work at thermal (*i.e.*, non-condensed) temperatures [14–16]. These interferometers, in the “Talbot-Lau” configuration, confine the atomic sample in two directions and allow free propagation in the third. In an ideal situation, the potential along the third direction would vanish. However, due to the finite size of the device and uncontrollable external fields, there is residual potential along the waveguide.

Unfortunately, the residual potential and other field imperfections reduce coherence times [13,17,18]. Recent research has demonstrated a high degree of control over the residual field [19]. Here, we analyze the effect of a controlled residual potential in a Talbot-Lau interferometer with a gas of cold, thermal atoms using a Wigner function approach.

## 2. Interferometer Operation

To prepare the atomic gas for the interferometer cycle, a laser cooled sample is loaded into a magnetic trap with frequencies  $\omega_i^{(e)}$ , where  $i = (x, y, z)$ . The collision rate is directly proportional to the geometric average of these trap frequencies  $\bar{\omega}^{(e)} = (\omega_x^{(e)}\omega_y^{(e)}\omega_z^{(e)})^{1/3}$ , so  $\bar{\omega}^{(e)}$  should be made as large as possible to maximize the efficiency of the evaporative cooling. In typical atom chip experiments, the gas is evaporatively cooled in a trap with frequency  $\bar{\omega}^{(e)} \sim 2\pi \times 200$  Hz.

Once the atoms are cooled to a temperature on the order of  $\mathcal{T} \sim 10$   $\mu$ K, the potential is adiabatically transformed into a trap that tightly confines the atoms in the radial direction, with frequencies  $\omega_y = \omega_z = \omega_{\perp} \sim 2\pi \times 200$  Hz; and in the axial direction, with frequency  $\omega_x = \omega_0$ . Just before the interferometer cycle starts, the potential is non-adiabatically transformed into a waveguide potential, while holding the radial trap frequency constant to reduce the effects of transverse excitations. In a realistic device, there remains a residual potential along the waveguide with frequency  $\omega$ .

Once the atoms are loaded in the waveguide, the interferometer cycle begins. In this analysis, we considered the case of the trapped atom Talbot-Lau interferometer schematically shown in Figure 1. The figure traces the different paths that an initially stationary atom could experience when moving through the device. Time moves from left to right, and the displacement of the atom along the waveguide is shown in the vertical direction.

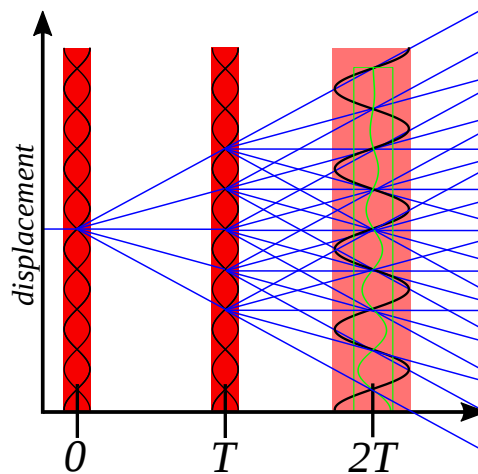


**Figure 1.** The schematic of a Talbot-Lau interferometer. An atomic cloud is split in space (vertical axis) by a laser pulse at time  $t = 0$ . The resulting diffracted orders separate, and are further diffracted at  $t = T$ . At the recombination time  $t = 2T$ , the various orders overlap, allowing a probe laser to produce a back scattered signal from the periodic atomic distribution. We only show two diffraction orders because for typical laser pulses, higher orders are suppressed.

At time  $t = 0$ , the atomic cloud is illuminated with a short, standing wave laser pulse that acts as a diffraction grating. The pulse is sufficiently short that it is in the Kapitza-Dirac regime, *i.e.*, the atoms do not move for the duration of the laser pulse. The pulse splits the wave function for each atom into several momentum states separated by the two photon recoil momentum  $\delta P = 2\hbar k_l$ , where  $k_l$  is the wave number of the laser beams.

After the laser pulse, the atomic cloud propagates in the waveguide for a time  $T$ , at which point it is illuminated with a second laser pulse. The paths of the different momentum states are shown as blue lines between 0 and  $T$ . Ideally, the momentum of each mode should be constant in time. However, the residual curvature along the waveguide will cause the paths to become curved (not shown in the figure), giving rise to decoherence.

For simplicity, it is assumed that the laser pulse at time  $T$  has the same strength and affects the atomic wave function in the same manner. Each of the momentum states that were populated after the

first laser pulse are split into several modes. After the second laser pulse, the number of possible paths increases dramatically. However, near time  $2T$ , the different paths come together to form a density modulation that has the same period as the standing wave.

An extraordinary feature of a Talbot-Lau interferometer is that the location of the density echo is independent of the initial velocity of the atom. For example, if the initial atom in Figure 1 had some momentum, each of the diffracted orders would maintain this additional momentum. After tracing out all possible paths, it is easy to show that the density modulation appears in exactly the same location as for the initially stationary atom. As a result, the density echo is still visible even when the initial atomic gas is relatively hot.

In the absence of external forces, the density echo will have the same relative phase as the standing wave laser pulse. However, if there is a force on the cloud, the echo will move in response to the force. By detecting the shift in the echo, it is possible to measure the force on the cloud.

This phase shift can be measured by reflecting a traveling wave off the density modulation. Due to the Bragg effect, there will be a strong backscattered signal for the duration of the echo. By heterodyning the back-reflected light with a reference beam, the phase of the density echo can be determined.

In this paper, we present a theoretical model of a trapped Talbot-Lau interferometer that includes the decoherence due to the residual potential curvature. We use the Wigner function approach to model the dynamics of a thermal gas, which can be extended to include more complex laser pulse sequences [18]. For brevity, only the simple case of a two-pulse interferometer is discussed. Our model predicts the amplitude of backscattered light for an arbitrary initial Wigner function and is then specialized to the case of an initial thermal distribution. Decoherence due to finite temperature and initial axial trap frequency are discussed. Finally the model is used to determine the ideal axial frequency for a given initial phase space density and residual potential.

### 3. The Model

Following the prescription of [19], we assume that the potential is separable, *i.e.*,  $V(\mathbf{r}) = V(x) + V_{\perp}(r_{\perp})$ , and the  $k$ -vectors of the laser beams point in the  $x$ -direction. Collisions are neglected as we have previously analyzed the effects of collisions in a similar interferometer and do not expect atom-atom collisions to have a significant impact on the results [20]. We also ignore the mean field interaction, as it is mainly relevant for strongly interacting condensates, which we do not consider here. Inclusion of these terms may be possible, but are omitted to keep the discussion concise. The Hamiltonian that governs the axial dynamics of the interferometer is one-dimensional and can be written as

$$H = \frac{P^2}{2M} + \frac{1}{2}M\beta X^2 + \hbar\Omega \cos(2k_l X), \quad (1)$$

where  $X$  and  $P$  are the canonical operators with commutation relation  $[X, P] = i\hbar$ ,  $k_l$  is the wave number of the laser,  $M$  is the atomic mass, and  $\beta$  is the curvature of the residual potential. The parameter  $\Omega$  is the frequency of the AC-stark shift due to the standing wave laser pulse, which depends on the intensity and detuning of the beam and is, in general, a function of time.

The Hamiltonian can be recast in the dimensionless form

$$H' = \frac{P'^2}{2} + \frac{1}{2}\beta' X'^2 + \Omega' \cos X', \quad (2)$$

where  $P' = P/P_0$ ,  $X' = X/X_0$ , and  $t' = t/t_0$  where  $P_0 = 2\hbar k_l$ ,  $X_0 = 1/2k_l$ , and  $t_0 = M/4\hbar k_l^2$ . The other parameters in Equation (1) become  $\beta' = \beta t_0^2$  and,  $\Omega' = \Omega t_0$ . The other important dimensionless parameter is the cloud temperature  $\mathcal{T}' = \mathcal{T}/\mathcal{T}_0$ , where  $\mathcal{T}_0 = 4\hbar^2 k_l^2 / M k_B$ , where  $k_B$  is the Boltzmann constant. For  $^{87}\text{Rb}$  where the standing wave laser is near the D2 transition,  $t_0 = 5.3 \mu\text{s}$ , and  $\mathcal{T}_0 = 1.4 \mu\text{K}$ . For the rest of this paper, primes will be dropped for clarity, and unless otherwise stated, all introduced variables will be dimensionless.

Since the interferometer uses an incoherent gas, the state of the system cannot be written as a wave function. Instead, the system is described by the density operator  $\rho$ . The equation of motion for the density operator, in dimensionless form, is

$$i\dot{\rho} = [H, \rho], \tag{3}$$

where the dot denotes the time derivative and the brackets are the usual commutation operator. The density operator can be recast in terms of the Wigner function, which is defined as

$$f(x, p) = \frac{1}{\pi} \int d\tilde{\zeta} \langle x + \tilde{\zeta} | \rho | x - \tilde{\zeta} \rangle e^{-2ip\tilde{\zeta}} \tag{4}$$

where  $|x\rangle$  are the eigenvectors of the coordinate operator, *i.e.*,  $X|x\rangle = x|x\rangle$ . The Wigner function  $f(x, p)$  can be interpreted as the probability density, however for non-classical states the Wigner function may be negative. As a result,  $\int dx f = \mathcal{P}(p)$  is the momentum density of the cloud and  $\int dp f = \rho(x)$  is the spatial density. Even when the Wigner function is negative, the densities,  $\mathcal{P}$  and  $\rho$  are always positive.

It is worth noting that the Wigner approach works for pure states as well. In this case, it is defined as

$$f_{\text{pure}}(x, p) = \frac{1}{\pi} \int d\tilde{\zeta} \psi^*(x + \tilde{\zeta}) \psi(x - \tilde{\zeta}) e^{-2ip\tilde{\zeta}}. \tag{5}$$

We will find that the results of the incoherent process are easily extended to include the results of a pure state (BEC) interferometer.

Substituting Equation (4) into Equations (2) and (3) it can be shown that the equation of motion for the Wigner function is

$$\left( \frac{\partial}{\partial t} + p \frac{\partial}{\partial x} - \beta \frac{\partial}{\partial p} \right) f(x, p, t) = \Omega \sin x \left[ f\left(x, p - \frac{1}{2}\right) - f\left(x, p + \frac{1}{2}\right) \right], \tag{6}$$

where the left side of the equation describes the motion of the distribution in the potential while the right side describes the interaction with the standing wave laser field.

Since the duration of the laser pulses  $\tau_p$  is much shorter than the interferometer time  $T$  ( $T \gg \tau_p$ ), the evolution of the distribution can be separated into relatively slow dynamics when the distribution is not being illuminated and fast dynamics when it is. Additionally, since each laser pulse is short  $\tau_p \gg 1/\omega_0$  and strong  $\Omega \gg \omega_0$ , the pulses are in the Kapitza-Dirac regime, which occurs in the Raman-Nath limit. As a result, the coordinate and momentum derivatives in Equation (6) may be neglected during the pulse.

The dynamics of the distribution for the periods when the laser is off,  $\Omega = 0$ , are such that each part of phase space evolves classically. For simplicity, it is useful to write the classical equations of motion in the form

$$\dot{\mathbf{x}} = M\mathbf{x} \tag{7}$$

where  $\mathbf{x} = (x, p)$  is the coordinate-momentum vector, and the matrix  $M$  is

$$M = \begin{pmatrix} 0 & 1 \\ -\beta & 0 \end{pmatrix}. \tag{8}$$

The solution to Equation (7) can be written as  $\mathbf{x}(t) = U_t \mathbf{x}(0)$ , where  $U_t = \exp(Mt)$ . By direct substitution it can be shown that in between the laser pulses the distribution evolves as

$$f_f(\mathbf{x}) = f_i(U_{-t}\mathbf{x}). \tag{9}$$

The laser pulses are more involved and fundamentally quantum in nature (*i.e.*, resulting in negative Wigner distributions). The effect of the laser pulse is to transform an initial Wigner distribution  $f_i$  into a final distribution  $f_f$  according to

$$f_f(\Omega \neq 0) = \sum_{nk=-\infty}^{\infty} (-i)^n J_k(\Xi) J_{n+k}(\Xi) e^{i(n+2k)x} f_i\left(x, p - \frac{n}{2}\right) \quad (10)$$

for the pulse area,  $\Xi = \int d\tau \Omega(\tau)$ , where the functions  $J_n$  are the Bessel functions of the first kind. In terms of  $\mathbf{x}$ , Equation (10) can be written in the more compact form

$$f_f(\Omega \neq 0) = \sum_{nk} \alpha_{nk} e^{i\mathbf{g}_{nk} \cdot \mathbf{x}} f_i(\mathbf{x} - \mathbf{N}_n) \quad (11)$$

where  $\mathbf{g}_{nk} = (n + 2k, 0)$ ,  $\mathbf{N}_n = (0, n/2)$ , and  $\alpha_{nk} = (-1)^n J_k J_{n+k}$ .

The interferometer sequence is characterized by four unique operations separated in time. The first laser pulse at  $t = 0$  operates on an initial Wigner distribution  $f_0$  and transforms it to  $f_1$  ( $f_0 \rightarrow f_1$ ). There is then a propagation period from  $t = 0$  to  $T$ , over which the distribution transforms  $f_1 \rightarrow f_2$ . The second laser pulse at  $t = T$  transforms  $f_2 \rightarrow f_3$ . Lastly, another propagation to  $t = 2T + \tau$  transforms the distribution to its final form  $f_3 \rightarrow f_4$ .

Near the end of the interferometer cycle, the cloud is illuminated with a short traveling wave laser pulse of duration  $\tau_0$ , where  $\tau_0 \ll T$ . To determine the time dependence of the back-scattered light, the Wigner function must be found for times near the echo time, *i.e.*,  $t = 2T + \tau$ . By direct substitution into Equations (9) and (11) for the interferometer cycle discussed in Figure 1, the Wigner function near the echo time is

$$\begin{aligned} f_4 = & \sum_{mlnk} \alpha_{ml} \alpha_{nk} \\ & \times \exp [i(\mathbf{g}_{ml} \cdot U_T + \mathbf{g}_{nk}) \cdot U_{-2T-\tau} \cdot \mathbf{x} - i\mathbf{g}_{nk} \cdot U_{-T} \cdot \mathbf{N}_m] \\ & \times f_0(U_{-2T-\tau} \cdot \mathbf{x} - U_{-T} \cdot \mathbf{N}_m - \mathbf{N}_n). \end{aligned} \quad (12)$$

According to [17], the amplitude of the back-scattered light is proportional to

$$S = \int d^2x e^{i\mathbf{g}_0 \cdot \mathbf{x}} f_4(\mathbf{x}). \quad (13)$$

For the rest of the paper, the quantity  $S$  will be referred to as the signal of the interferometer. Changing the integration variable from  $\mathbf{x}$  to  $\mathbf{y}$ , where

$$\mathbf{y} = U_{-2T-\tau} \mathbf{x} - U_{-T} \mathbf{N}_m - \mathbf{N}_n, \quad (14)$$

the signal can be written as

$$S = \sum_{mlnk} \alpha_{ml} \alpha_{nk} e^{i\Theta_{mlnk}} \int d^2y e^{i\Delta_{mlnk} \cdot \mathbf{y}}, \quad (15)$$

where

$$\Delta_{mlnk} = \mathbf{g}_{ml} \cdot U_T + \mathbf{g}_{nk} + \mathbf{g}_{10} \cdot U_{2T+\tau}, \quad (16)$$

and

$$\Theta_{mlnk} = \Delta_{mlnk} \cdot (U_{-T} \cdot \mathbf{N}_m + \mathbf{N}_n) - \mathbf{g}_{nk} \cdot U_{-T} \cdot \mathbf{N}_m. \quad (17)$$

In what follows below, it will be assumed that both the echo duration is small as compared to the interferometer time  $\tau \ll T$ , and the residual trap curvature is  $\beta \ll 1/T^2$ . When these inequalities are fulfilled, only the linear contributions in both  $\tau$  and  $\beta$  are retained. In this limit, the time propagation operator for small values of  $\beta$  is  $U_T \approx U_T^{(0)} + \beta U_T^{(1)}$ , where  $U_t^{(0)} = \begin{pmatrix} 1 & t \\ 0 & 1 \end{pmatrix}$ , and  $U_t^{(1)} = \begin{pmatrix} t^2/2 & t^3/6 \\ t & t^2/2 \end{pmatrix}$ , and for small values of time  $\tau$ ,  $U_\tau = 1 + M^{(1)}\tau$ , where  $M^{(1)} = \begin{pmatrix} 0 & 1 \\ 0 & 0 \end{pmatrix}$ .

Equation (16) can now be written as

$$\Delta_{mlnk} = \Delta_{mlnk}^{(0)} + \beta \left( \mathbf{g}_{ml} \cdot U_T^{(1)} + \mathbf{g}_{10} \cdot U_{2T}^{(1)} \right) + \tau \left( \mathbf{g}_{10} U_{2T}^{(0)} M^{(1)} \right), \quad (18)$$

where  $\Delta^{(0)}$  is given by Equation (16) where  $\beta \rightarrow 0$  and  $\tau \rightarrow 0$ . In the limit where the distribution is slowly varying, the elements of the sum in Equation (13) are vanishingly small unless  $\Delta^{(0)} = 0$ . This implies that  $\mathbf{g}_{ml} = -2\mathbf{g}_{10}$  and  $\mathbf{g}_{nk} = \mathbf{g}_{10}$ . Using the definition of  $\mathbf{g}$ , these relations can be written as  $k = (1 - n)/2$  and  $l = -(2 + m)/2$ . In addition, only the terms where  $n, (m)$  are even (odd) contribute to the signal. Equation (18) becomes independent of the indices  $m, l, n, k$ .

Substituting the explicit matrix representations for  $\Delta$  and  $\Theta$ , the interferometer signal is given by

$$S = A \int dudv \exp \left[ -i\beta T^2 u + i\tau' v \right] f_0(u, v), \tag{19}$$

where  $\tau' = \tau - \beta T^3$  and  $u, v$  are the components of the vector  $\mathbf{y}$ . The parameter  $A$  in Equation (19) is the amplitude of the signal and can be expressed as the sum

$$A = \sum_{n, \text{even}} \sum_{m, \text{odd}} \frac{\gamma_{nm}}{2i} \exp \left[ i \left( \frac{mT}{2} + \frac{m+n}{2} \tau' + \frac{5m}{12} \beta T^3 \right) \right], \tag{20}$$

where

$$\gamma_{nm} = 2(-1)^{(n-1)/2+m/2} J_{(1-n)/2} J_{(1+n)/2} J_{-(2+m)/2} J_{-(2-m)/2} \tag{21}$$

determines proportion of the atoms scattered into each mode.

Equation (19) is the primary result of this analysis, and will be used for the case of a thermal atomic cloud in Section 4.

#### 4. Discussion

By taking the limit where  $\Xi \ll 1$ , only the lowest order contributions to Equation (20) need to be retained. If we keep  $n = \pm 1$  and  $m = 0, \pm 2$  and use the limiting values of  $J_n$  for the small argument,  $\gamma_{10} \approx -2\gamma_{12} \approx \Xi/4$ , then

$$A = \sin \left( \frac{1}{2} \tau' \right) \frac{\Xi^3}{4} \left[ 1 + \cos \left( T + \frac{5\beta T^3}{6} + \tau' \right) \right]. \tag{22}$$

Assuming that the initial distribution is a thermal cloud of temperature  $\mathcal{T}$  that is in equilibrium with the trap with frequency  $\omega_0$ , the distribution  $f_0$  becomes

$$f_0 = \frac{\omega_0}{2\pi\mathcal{T}} \exp \left( -\frac{p^2}{2\mathcal{T}} - \frac{\omega_0^2 x^2}{2\mathcal{T}} \right). \tag{23}$$

By comparison, the initial distribution of a condensate would be well approximated by the ground state of a harmonic oscillator. Using Equation (5), the pure state Wigner function is equivalent to Equation (23) when  $\mathcal{T} = \omega_0/2$ . During the transition from an incoherent thermal gas to a pure BEC, the distribution is a sum of  $f_0$  and  $f_{\text{pure}}$ , weighted by the number of atoms in and out of the ground state, where  $N_0/N = 1 - (\mathcal{T}/\mathcal{T}_c)^3$  and  $\mathcal{T}_c = \bar{\omega}_0(N/\zeta(3))^{1/3}$ .  $N_0/N$  is the ratio of condensed atoms to the total, and  $\zeta$  is the Riemann zeta function. This combined distribution can be used with Equation (19) to find the expected signal.

Returning focus to the incoherent thermal gas, substituting Equations (22) and (23) into Equation (19) and performing the integral yields

$$S = A \exp \left[ -\frac{\mathcal{T}}{2} \left( \frac{\beta T^2}{\omega_0} \right)^2 - \frac{\mathcal{T}}{2} \tau'^2 \right]. \tag{24}$$

To quantify the signal visibility, we define the echo strength as  $\mathcal{I} = \Xi^6 \int d\tau' S^2$ , which is proportional to the total number of photons (electromagnetic energy) of the backscattered light during the read-out pulse. In the limit where  $\mathcal{T} \gg 1$ , Equation (24) can be integrated, yielding

$$\mathcal{I} = \frac{\pi^{1/2} \mathcal{A}^2}{32\mathcal{T}^{3/2}} \exp \left[ -\mathcal{T} \left( \frac{\beta T^2}{\omega_0} \right)^2 \right], \quad (25)$$

where

$$\mathcal{A} = \frac{1}{4} \left[ 1 + \cos \left( T + \frac{5}{6} \beta T^3 \right) \right]. \quad (26)$$

Equation (25) appears to diverge in the limit  $\mathcal{T} \rightarrow 0$ , which is clearly an unphysical result. However the numerical integration of Equation (24) remains finite.

Note that  $\mathcal{I}$  is an oscillating function, and is well known in the  $\beta = 0$  case [3]. Figure 2 shows a schematic of Equation (25) as a function of interferometer time  $T$  for  $\beta > 0$ . The dotted line is the envelope of the echo strength. Figure 3 shows a schematic of Equation (25) as a function of interferometer time  $T$  for  $\beta < 0$ .

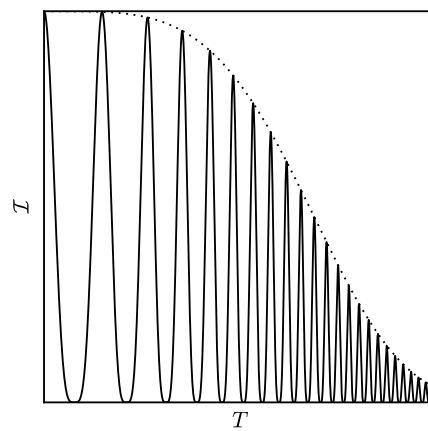


**Figure 2.** A schematic of the echo signal strength,  $\mathcal{I}$ , as a function of interferometer time,  $T$ , for an interferometer in a positive residual trapping potential, *i.e.*,  $\beta > 0$ . The signal strength is proportional to the total number of backscattered photons during the readout laser pulse.  $\mathcal{I}$  is periodic with an increasing frequency within an envelope defined by the dotted curve.

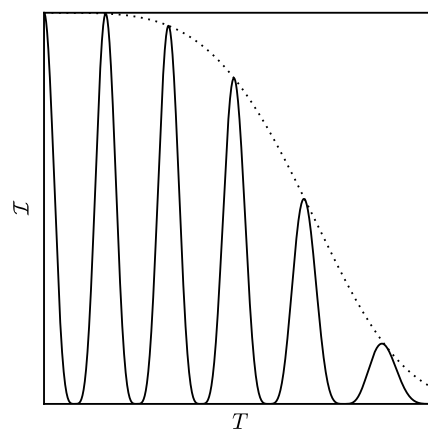


**Figure 3.** A schematic of the echo signal strength,  $\mathcal{I}$ , as a function of interferometer time,  $T$ , for an interferometer in a negative residual trapping potential, *i.e.*,  $\beta < 0$ . Like the positive potential case, the signal strength is periodic and contained within a decaying envelope. However, the negative potential causes a decreasing frequency. Both positive and negative potentials have the same envelope.

The oscillation frequency increases when  $\beta > 0$  and decreases when  $\beta < 0$ , and there is a maxima when  $T + 5\beta T^3/6 = 2\pi n$ . These oscillations depend only on the values of  $\beta$  and  $T$ . In a typical

experiment, the oscillation frequency is much larger than depicted in Figure 2 or Figure 3. For the remainder of the paper, it will be assumed that the interferometer time is tuned to be at the peak of an oscillation, which will be referred to as  $\mathcal{I}_m$ .

In order to maximize signal strength, it is also useful to release the atomic sample into the waveguide from the correct initial trap. Typically, the atomic gas is evaporatively cooled to a temperature  $\mathcal{T}^{(e)}$  in a trap with frequency  $\omega^{(e)}$ . After cooling, the trap frequencies are adiabatically changed to a trap with frequency  $\omega_0$  and then released into a waveguide with residual potential curvature  $\beta$ . During the adiabatic transformation, the phase space density is constant. This condition implies  $D = \mathcal{T}^3/\omega$  is held constant, assuming the radial trap frequencies  $\omega_{\perp}$  are unchanged. Then Equation (25) can be recast as

$$\mathcal{I}_m = \frac{\pi^{1/2}}{32(D^{(e)})^2\omega_0^2} \exp \left[ -\frac{(D^{(e)})^{1/3}}{\omega_0^{5/3}} (\beta T^2)^2 \right], \quad (27)$$

where  $D^{(e)} = (\mathcal{T}^{(e)})^3/\omega^{(e)}$  is proportional to the phase space density at the end of the evaporation.

For this analysis, assume the cloud is evaporatively cooled in a trap with frequency  $\omega^{(e)} = 2\pi \times 10^{-4}$  and to a temperature  $\mathcal{T} = 10$ . For  $^{87}\text{Rb}$ , these parameters correspond to a gas cooled in a trap with a frequency of 20 Hz to a temperature of 14  $\mu\text{K}$ . The phase space density is proportional to  $D^{(e)} = 10^{-6}/2\pi$ . Figure 4 shows the echo strength, Equation (27), as a function of decompressed trap frequency  $\omega_0$ . The remaining parameter  $|\beta|^{1/2}T = 10^{-2}$ , corresponds to a cycle time of 10 ms and a residual frequency of 0.3 Hz. In this case, the decompressed trap frequency is roughly half the evaporative trap frequency.

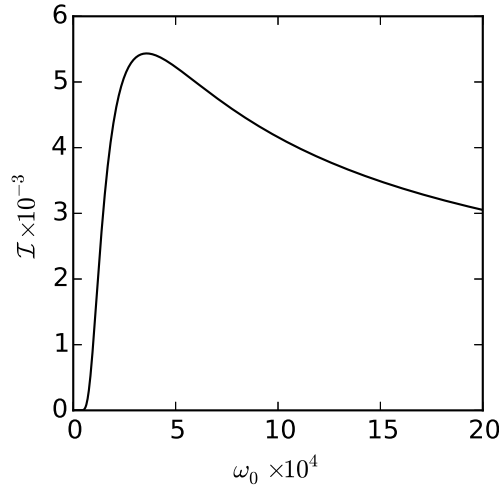


**Figure 4.** The signal strength as a function of injection trap frequency,  $\omega_0$ . After evaporation in a trap with frequency  $\omega^{(e)}$ , the trap potential is adiabatically transformed to  $\omega_0$  before the interferometer cycle begins. At the start of the cycle, the trap is snapped to  $\omega = \sqrt{\beta}$ , where it stays. The signal strength peaks at for a non-zero injection frequency  $\omega_0$ . For this case,  $\beta T^2 = 10^{-4}$ , and  $D^{(e)} = 10^6/2\pi$ .

For small values of  $\omega_0 \ll 1$ , the echo strength vanishes because the weak trap creates a large cloud, which experiences more de-phasing due to the residual potential. On the other hand, when  $\omega_0 \gg 1$ , the echo strength vanishes because the tight trap increases the temperature of the cloud, resulting in a shorter echo duration.

The ratio of ideal starting trap frequency  $\omega_0$  and evaporation trap frequency  $\omega^{(e)} = 2\pi \times 10^{-3}$  is shown as a function of  $|\beta|^{1/2}T$  in Figure 5. The dash-dot line is the ideal frequency if the gas is cooled to a temperature of  $\mathcal{T} = 1$ , the solid line is the ideal frequency when  $\mathcal{T} = 10$ , and the dashed line is when  $\mathcal{T} = 20$ .



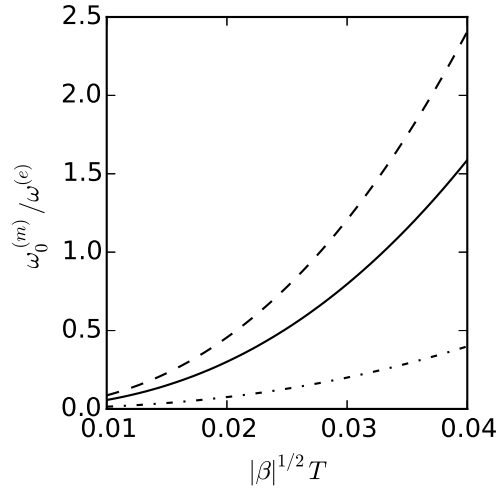


**Figure 5.** The ratio of the ideal injection trap frequency,  $\omega_0$ , to the evaporation trap frequency,  $\omega^{(e)}$ , as a function of  $|\beta|^{1/2}T$ . Here we use  $\omega^{(e)} = 2\pi \times 10^{-3}$ , and plot for temperatures  $T = 1$  (dash-dot),  $T = 10$  (solid), and  $T = 20$  (dash). As the ratio  $\omega_0/\omega^{(e)}$  becomes greater than one, the gas should be compressed before being released into the interferometer. This compression step raises the temperature, but reduces the size of the cloud.

For values where  $\omega_0/\omega_e < 1$ , the ideal starting frequency is lower than the evaporation frequency, *i.e.*, the gas should be decompressed before the beginning of the interferometer cycle. At the cost of increasing the cloud size, it is more advantageous the lower the temperature. For the case where  $\omega_0/\omega_e > 1$ , the gas should be compressed, raising the temperature by reducing the size of the cloud.

### 5. Outlook

Tuning the interferometer time  $T$  and the injection trap frequency  $\omega_0$  allows for maximal signal visibility. However, these optimizations cannot overcome the  $\exp(-\beta^2)$  dependence in Equation (25). Even a small residual potential dramatically reduces coherence times in this version of a trapped Talbot-Lau interferometer. Figure 6 shows the signal visibility, Equation (25), for several residual potentials. The dashed curve is  $\beta = 5 \times 10^{-13}$ , the solid line is  $10^{-12}$ , and the dash-dot curve is  $10^{-11}$ . For this plot,  $\mathcal{I}_0 = \pi^{1/2} \mathcal{A}^2 / 32 T^{3/2}$ , with  $\mathcal{A} = 1/2$  to correspond to maxima in the signal oscillation. For the time axis,  $T \times 10^{-2}$  corresponds roughly to 1 ms.

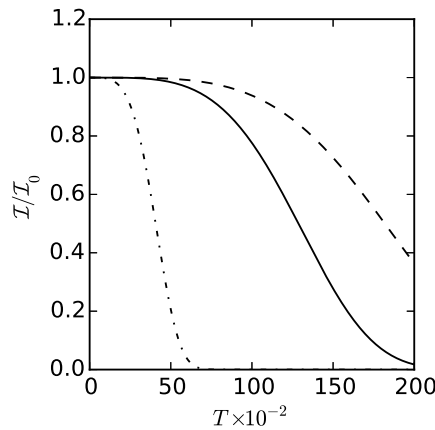


**Figure 6.** The signal visibility, *i.e.*, the decaying envelope that limits the maximum possible signal strength for a given interferometer time  $T$ . The decay is proportional to  $\exp(-\beta^2)$ , causing rapid signal loss for even small residual potentials. Here we show  $\beta = 5 \times 10^{-13}$  (dashed),  $10^{-12}$  (solid), and  $10^{-11}$  (dash-dot).  $T \times 10^{-2}$  corresponds roughly to 1 ms.

Clearly the signal visibility has a strong dependence on residual potential, which must be extremely small for coherence times compared to free space interferometers. In future work, we will explore modifications to the trapped Talbot-Lau scheme with the potential to minimize the coherence time's sensitivity on residual field imperfections.

The Wigner function approach allows a straightforward way to model interference in an incoherent system such as a cold atomic gas. It can be readily applied to consider different pulse schemes such as those of [17], as well as propagation in more complex confining potentials. The Talbot-Lau interferometer's ability to operate at thermal temperatures is a significant enough benefit to a real-world device that further study is warranted.

**Acknowledgments:** This work was supported by the Air Force Research Laboratory.

**Author Contributions:** Eric Imhof, James Stickney, and Matthew Squires contributed equally to this paper. All authors have read and approved the final version.

**Conflicts of Interest:** The authors declare no conflict of interest.

## References

1. Barrett, B.; Chan, I.; Kumarakrishnan, A. Atom-interferometric techniques for measuring uniform magnetic field gradients and gravitational acceleration. *Phys. Rev. A* **2011**, *84*, 063623.
2. Muntinga, H.; Ahlers, H.; Krutzik, M.; Wenzlawski, A.; Arnold, S.; Becker, D.; Bongs, K.; Dittus, H.; Duncker, H.; Gaaloul, N.; *et al.* Interferometry with Bose-Einstein Condensates in Microgravity. *Phys. Rev. Lett.* **2013**, *110*, 093602.
3. Cahn, S.B.; Kumarakrishnan, A.; Shim, U.; Sleator, T.; Berman, P.R.; Dubetsky, B. Time-Domain de Broglie Wave Interferometry. *Phys. Rev. Lett.* **1997**, *79*, 784–787.
4. Cronin, A.; Schmiedmayer, J.; Pritchard, D. Optics and interferometry with atoms and molecules. *Rev. Mod. Phys.* **2009**, *81*, 1051–1129.
5. Adams, C.; Sigel, M.; Mlynek, J. Atom optics. *Phys. Rep.* **1994**, *240*, 143–210.
6. Geiger, R.; Menoret, V.; Stern, G.; Zahzam, N.; Cheinet, P.; Battelier, B.; Villing, A.; Moron, F.; Lours, M.; Bidet, Y.; *et al.* Detecting inertial effects with airborne matter-wave interferometry. *Nat. Commun.* **2011**, *2*, 474.
7. Durfee, D.; Shaham, Y.; Kasevich, M. Long-term stability of an area-reversible atom-interferometer Sagnac gyroscope. *Phys. Rev. Lett.* **2006**, *97*, 240801.
8. Dickerson, S.M.; Hogan, J.M.; Sugarbaker, A.; Johnson, D.M.S.; Kasevich, M.A. Multiaxis Inertial Sensing with Long-Time Point Source Atom Interferometry. *Phys. Rev. Lett.* **2013**, *111*, 083001.
9. Wang, Y.; Anderson, D.; Bright, V.; Cornell, E.; Diot, Q.; Kishimoto, T.; Prentiss, M.; Saravanan, R.; Segal, S.; Wu, S. Atom Michelson interferometer on a chip using a Bose-Einstein condensate. *Phys. Rev. Lett.* **2005**, *94*, 090405.
10. Schumm, T.; Kruger, P.; Hofferberth, S.; Lesanovsky, I.; Wildermuth, S.; Groth, S.; Bar-Joseph, I.; Andersson, L.M.; Schmiedmayer, J. A Double Well Interferometer on an Atom Chip. *Quantum Inf. Process.* **2006**, *5*, 537–558.
11. Hilico, A.; Solaro, C.; Zhou, M.K.; Lopez, M.; Pereira dos Santos, F. Contrast decay in a trapped-atom interferometer. *Phys. Rev. A* **2015**, *91*, 053616.
12. Horikoshi, M.; Nakagawa, K. Dephasing due to atom-atom interaction in a waveguide interferometer using a Bose-Einstein condensate. *Phys. Rev. A* **2006**, *74*, 031602.
13. Burke, J.; Sackett, C. Scalable Bose-Einstein-condensate Sagnac interferometer in a linear trap. *Phys. Rev. A* **2009**, *80*, 061603.
14. Wu, S.; Su, E.; Prentiss, M. Time domain de Broglie wave interferometry along a magnetic guide. *Eur. Phys. J. D* **2005**, *35*, 111–118.
15. Xiong, W.; Zhou, X.; Yue, X.; Chen, X.; Wu, B.; Xiong, H. Critical correlations in an ultra-cold Bose gas revealed by means of a temporal Talbot-Lau interferometer. *Laser Phys. Lett.* **2013**, *10*, 125502.
16. Mok, C.; Barrett, B.; Carew, A.; Berthiaume, R.; Beattie, S.; Kumarakrishnan, A. Demonstration of improved sensitivity of echo interferometers to gravitational acceleration. *Phys. Rev. A* **2013**, *88*, 023614.

17. Wu, S. *Light Pulse Talbot-Lau Interferometry with Magnetically Guided Atoms*; Harvard University: Cambridge, MA, USA, 2007.
18. Su, E.; Wu, S.; Prentiss, M. Atom interferometry using wave packets with constant spatial displacements. *Phys. Rev. A* **2010**, *81*, 043631.
19. Stickney, J.; Kasch, B.; Imhof, E.; Kroese, B.; Crow, J.; Olson, S.; Squires, M. Tunable axial potentials for atom chip waveguides. 2014, arXiv:1407.6398.
20. Stickney, J.; Squires, M.; Scoville, J.; Baker, P.; Miller, S. Collisional decoherence in trapped-atom interferometers that use nondegenerate sources. *Phys. Rev. A* **2009**, *79*, 013618.



© 2016 by the authors; licensee MDPI, Basel, Switzerland. This article is an open access article distributed under the terms and conditions of the Creative Commons Attribution (CC-BY) license (<http://creativecommons.org/licenses/by/4.0/>).